

Dynamical Constraints on the Vertical Structure of Jupiter’s Polar Cyclones

Nimrod Gavriel^{1*} and Yohai Kaspi¹

¹*Department of Earth and Planetary Sciences, Weizmann Institute of Science, Rehovot, Israel*

**nimrod.gavriel@weizmann.ac.il*

Preprint February 19, 2025

Abstract

Jupiter’s poles feature striking polygons of cyclones that drift westward over time—a motion governed by β -drift. This study investigates how β -drift and the resulting westward motion depend on the depth of these cyclones. Counterintuitively, shallower cyclones drift more slowly, a consequence of stronger vortex stretching. By employing a 2D quasi-geostrophic model of Jupiter’s polar regions, we constrain the cyclones’ deformation radius, a key parameter that serves as a proxy for their vertical extent, required to replicate the observed westward drift. We then explore possible vertical structures and the static stability of the poles by solving the eigenvalue problem that links the 2D model to a 3D framework, matching the constrained deformation radius. These findings provide a foundation for interpreting upcoming Juno microwave measurements of Jupiter’s north pole, offering insights into the static stability and vertical structure of the polar cyclones. Thus, by leveraging long-term motion as a novel constraint on vertical dynamics, this work sets the stage for advancing our understanding of the formation and evolution of Jupiter’s enigmatic polar cyclones.

arXiv:2502.12789v1 [astro-ph.EP] 18 Feb 2025

1 Introduction

Probing beneath the clouds of Jupiter

Historically, our understanding of Jupiter’s atmosphere has been limited to observations of its visible cloud layer, located near the 1-bar pressure level. This limitation arises from the challenges of probing beneath the optically thick ammonia and water clouds (Atreya et al., 1999; de Pater et al., 2016). Until recently, the only direct measurements of Jupiter’s subcloud layers were the localized and costly in-situ data collected by the Galileo Probe (Young, 1998). However, an indirect method using gravity measurements—by tracking changes in spacecraft acceleration during close flybys—has enabled insights into the large-scale flows at depth. This approach has revealed the 3D structure of zonal flows within Jupiter’s subequatorial jet streams (Kaspi et al., 2018; Galanti et al., 2021; Kaspi et al., 2023) and constrained the depth of the Great Red Spot to less than 500 km (Galanti et al., 2019; Parisi et al., 2021).

Another approach to exploring Jupiter’s subcloud layers involves observations at cloud-penetrating frequencies. For example, using radio frequencies, the Earth-based Very Large Array (VLA) telescopes have probed down to pressures of approximately 8 bars (de Pater et al., 2016).

A more transformative development in exploring Jupiter’s subcloud atmosphere came with the Juno spacecraft. Equipped with a 6-channel Microwave Radiometer (MWR), Juno has been providing spatially resolved observations of "brightness temperatures" down to depths of approximately 240 bars (Bolton et al., 2017; Janssen et al., 2017). These thermodynamic measurements are influenced both by temperature variations (Fletcher et al., 2021) and the opacity of ammonia clouds (Li et al., 2017). Although there is ongoing debate about the relative contributions of these factors, the observed deep patterns reveal valuable information about the vertical structure and depth of atmospheric phenomena seen at the cloud tops. For example, the MWR detected alternating zonal bands of ammonia depletion and enrichment extending to 240 bars between midlatitude jets. These patterns correspond to the upwelling and downwelling branches expected in a Ferrel-cell-like circulation (Duer et al., 2021, 2023).

Another significant instrument on Juno, the Jovian Infrared Auroral Mapper (JIRAM), was designed to study the aurora and atmospheric chemistry at 5-7 bar (Adriani et al., 2017). During Juno’s polar orbits, as JIRAM is insensitive to half the pole being dark and can wholly observe the pole, it discovered a new phenomenon: a polar "crystal" of massive cyclones (each $\sim 5,000$ km wide) inhabiting each pole, consisting of a polar cyclone (PC) and 8 circumpolar cyclones (CPCs) at the north pole, and 5 at the south (Adriani et al., 2018). The MWR instrument, designed to function optimally at the shorter distances from Jupiter’s cloud-tops during the around-equatorial skims in its original polar orbit, now enters a phase in Juno’s extended mission, where the orbit has considerably shifted, allowing MWR measurements in the north pole of Jupiter (Orton et al., 2024). This enables multi-channel measurements with

sufficient resolution to capture the north polar cyclones, similar to analogous previous measurements of vortices in the midlatitudes (Bolton et al., 2021). This paper aims to use these novel measurements to interpret the vertical structure and extent of Jupiter’s polar cyclones.

Jupiter’s Polar Cyclones

The energetic processes sustaining Jupiter’s polar cyclone configurations, while explored in prior studies (O’Neill et al., 2015; Brueshaber et al., 2019; Hyder et al., 2022; Siegelman et al., 2022b,a), remain largely unconstrained. Nevertheless, substantial progress has been made in understanding the steady-state momentum balance that governs these cyclones, explaining both their stability and long-term motion. This momentum balance is closely related to the concept of β -drift—a secondary effect that causes vortices to move due to their interaction with a background vorticity gradient (Sutyryn and Flierl, 1994) known to influence the motion of tropical cyclones on Earth (Franklin et al., 1996). The phenomenon of β -drift has been explored extensively in idealized settings, including theoretical studies (Adem, 1956; Smith and Ulrich, 1990), numerical simulations (Lam and Dritschel (2001); Gavriel and Kaspi (2023)), and laboratory experiments (Benzeggouta et al., 2025).

Traditionally, as suggested by the term " β -drift", studies have focused on the interaction of cyclones with β , the meridional gradient of the planetary vorticity f , causing a poleward-westward migration. However, in addition to β , cyclones on Jupiter’s poles exhibit mutual repulsion due to the interaction of the vorticity gradient of one cyclone with that of another. This mutual interaction allows for the stable crystal-like configuration of the cyclones (Gavriel and Kaspi, 2021), provided that they are surrounded by an anticyclonic annulus, commonly referred to as shielding (Li et al., 2020). This repulsion also explains the oscillatory motion of the polar cyclones (Gavriel and Kaspi, 2022), as observed by Juno (Mura et al., 2021).

Beyond oscillatory motion, the cyclones exhibit a mean westward drift, with rates of approximately 3° and 7° per year at the north and south poles, respectively (Adriani et al., 2020; Mura et al., 2022). This westward drift arises from the β -drift acting collectively on the group of cyclones. By adopting a "center of mass" perspective, the mutual interactions between the cyclones are effectively averaged out, leaving only the cumulative interaction of the group with β . This dynamic leads to a group oscillation around the poles accompanied by a westward precession, manifesting as the observed drift (Gavriel and Kaspi, 2023).

In this study, we investigate how the vertical structure and depth of Jupiter’s polar cyclones influence their mean westward drift. First, we employ an idealized 2D model to explore how depth—and the associated column stretching—affects β -drift on a vortex in a β -plane. Next, we perform a parameter scan using a 2D Quasi-Geostrophic (QG) polar model with Jupiter’s polar cyclones initialized in the system to constrain the QG deformation radius (L_d), a proxy for depth, such that the modeled

westward drift matches observational data. Finally, we solve the eigenvalue problem posed by comparing 2D and 3D QG systems to deduce the vertical structures and static stability of the polar cyclones based on the constrained L_d .

2 The Impact of Vertical Depth on Vortex β -Drift

A standard framework for understanding the motion of vortices due to β -drift is the barotropic quasi-geostrophic (QG) equation of a seeded vortex on a β -plane (Smith and Ulrich, 1990; Sutyris and Flierl, 1994; Smith, 1991). In this formulation, cyclones undergo poleward-westward propagation in a planetary β , with the drift amplitude scaling with the dimensionless parameter $\hat{\beta} = \frac{\beta R^2}{V}$ (Gavriel and Kaspi, 2023), where R and V are the characteristic size and velocity of the cyclone. In this section, we seek to understand how the vertical extent (through stretching) modifies the classical β -drift by adding the stretching term to the QG equation.

Following the derivation in Smith and Ulrich (1990) but including stretching (see supporting information for the scaling, derivation, and other details), we develop the equations in a reference frame moving with the center of the cyclone. The scaled resulting QG equation becomes (focusing on the most dominating terms)

$$\frac{\partial}{\partial t} \left(\xi_g - \frac{\psi_g}{\text{Bu}} \right) = -\hat{\beta} v_v - \mathbf{u}_v \cdot \nabla \xi_g, \quad (1)$$

where ξ and ψ are the vorticity and streamfunction, respectively, and $\mathbf{u} = (u, v)$ is the velocity vector. Subscripts v and g represent, respectively, a constant background vortex flow and a "generated" field leading to the β -drift. The Burger number, $\text{Bu} \equiv \left(\frac{L_d}{R} \right)^2$, incorporates the effect of the deformation radius, $L_d = \frac{\sqrt{gH}}{f_0}$, where g is gravitational acceleration, H is the layer depth, and f_0 is the Coriolis parameter. The term $-\frac{\partial}{\partial t} \left(\frac{\psi_g}{\text{Bu}} \right)$ captures the influence of stretching in the single-layer QG model.

The model is solved for vortex profiles of the form (Chan and Williams, 1987):

$$\xi_v = \frac{V}{R} \left(2 - \left(\frac{r_c}{R} \right)^b \right) \exp \left[\frac{1}{b} \left(1 - \left(\frac{r_c}{R} \right)^b \right) \right], \quad (2)$$

where r_c is the distance from the vortex's center, and b is a shape factor for the vortex. The initial-value problem is solved using the Dedalus PDE solver (Burns et al., 2020). The results from this model, as a function of Bu , are shown in Fig. 1. The zonal β -drift velocity, defined as $u_\beta \equiv u_g|_{(x=0, y=0)}$, displays an exponential decay, which is modeled by $A(1 - e^{-t/\tau})$ (Fig. 1a).

We further examine the dependence of the fitted maximum drift velocity (A) and timescale (τ) on layer depth (Fig. 1c) for three values of the shape factor b within a physically relevant

range. The results indicate that while the drift amplitude is relatively insensitive to changes in b , it becomes more negative (more strongly westward) as the Burger number increases (or equivalently, as H increases).

In Gavriel and Kaspi, 2023 (Gavriel and Kaspi, 2023) (their Fig. 2), the layer depth H is assumed to be infinite, which implies $L_d \rightarrow \infty$ and $\text{Bu} \rightarrow \infty$, effectively removing the stretching term from Eq. 1. This assumption highlights that for very deep layers, any change in the fluid upper surface height (δh) is negligible compared to the total depth ($\frac{\delta h}{H} \ll 1$), rendering stretching effects unimportant to the dynamics.

However, when H and Bu are finite, the formation of β -gyres (described by the term $\frac{\partial \xi_g}{\partial t}$ in Eq. 1) is weakened, since vorticity generation now competes with stretching effects. Consequently, shallower layers experience a greater influence of stretching, which reduces the β -drift. This trend is reflected in Fig. 1c, where shallower layers correlate with stronger stretching and hence smaller β -drift velocities.

Using the Jovian values for the north and south poles of $\hat{\beta}$, R , and V from Gavriel and Kaspi (2023), we find that matching the observed westward drift corresponds to $A = -0.46$ for the north pole and $A = -0.54$ for the south pole, marked in Fig. 1c. These values correspond to $\text{Bu} = 0.49$ for the north pole and $\text{Bu} = 0.59$ for the south, which is used in Fig. 1e to show the generated fields after five rotation periods. The influence of Bu extends beyond the reduction of the β -drift amplitude. Larger Bu values also extend the time required to reach the peak drift velocity (τ in Fig. 1c) and lead to a more zonal flow overall (α in Fig. 1d).

From $\text{Bu} = (0.49, 0.59)$ and $R = (811, 861)$ km, the resulting deformation radii are $L_d = (568, 658)$ km for the north and south poles, respectively. These values, however, represent simplified first estimates of L_d that do not account for interactions among cyclones or the radial dependence of the Coriolis parameter (f) at Jupiter's poles. In the next section, we consider these additional complexities to obtain a more realistic estimate of the L_d required to explain the observed drift rates.

3 Estimating the Deformation Radius Using a Single-Layer QG Model of the Jovian Poles

While the previous section focused on how vertical extent modifies β -drift, the idealized model used there does not provide a realistic estimate of L_d . To address this limitation, we now present a single-layer QG model initialized with a polar vortex crystal. This model evolves under the full spherical form of the vertical component of Jupiter's rotation rate, $f = 2\Omega \cos\left(\frac{r}{R_J}\right)$, where Ω is Jupiter's rotation rate, R_J is Jupiter's radius, and r is the distance from the pole. We use Dedalus (Burns et al., 2020) to solve the polar QG equation (Vallis, 2017):

$$\frac{D}{Dt} \left(\nabla^2 \psi + 2\Omega \cos\left(\frac{r}{R_J}\right) - \frac{1}{L_d^2} \psi \right) = 0, \quad (3)$$

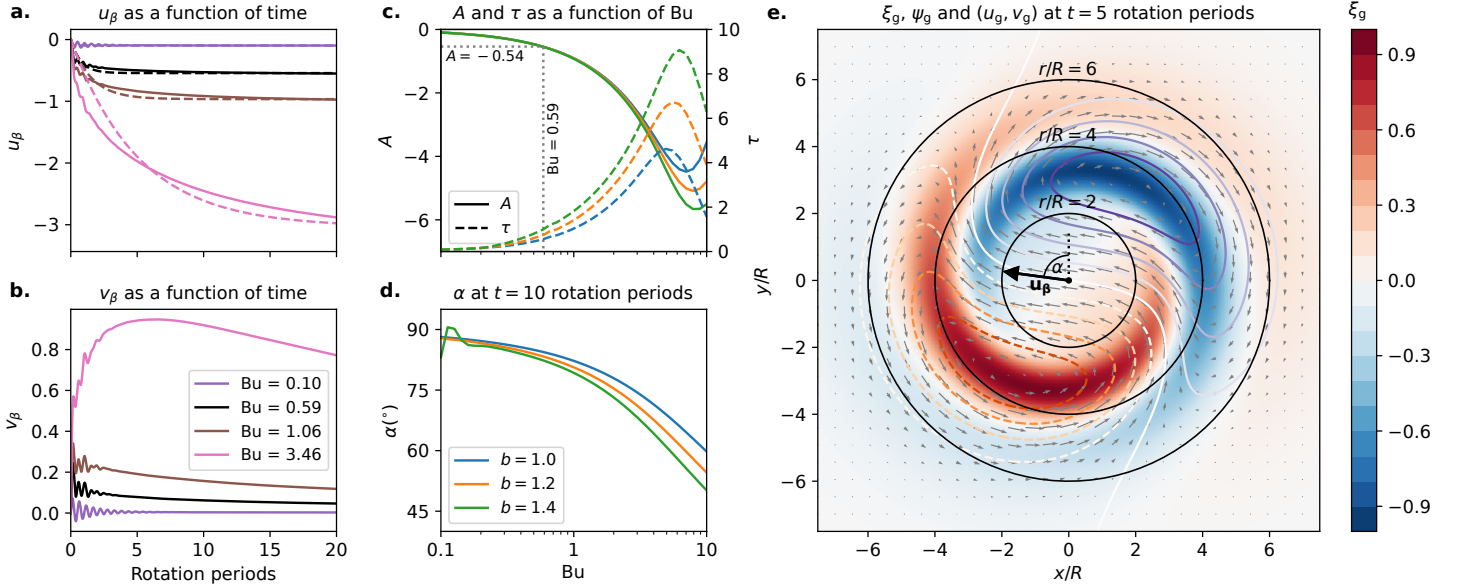


Figure 1: **Impact of Stretching on β -Drift Dynamics in a Single-Layer QG Framework.** (a–b) Evolution of the zonal (u_β) and meridional (v_β) drift velocities over time for four different values of the Burger number and $b = 1.2$. Dashed curves show exponential fits with amplitude A and timescale τ . Here, (u_β, v_β) are non-dimensional, scaled by $\hat{\beta}V$. (c) Plots of A (solid line, left axis) and τ (dashed line, right axis, in rotation periods) as functions of Bu for three values of the shape factor b , shown in panel (d). (d) The phase angle α (defined in panel e) between u_β and v_β vs. Bu . (e) The vorticity field (ξ_g , in color), streamfunction (ψ_g , in contours), and velocity field (\mathbf{u}_g , arrows) after five rotation periods for $Bu = 0.59$. The colorbar represents the scaled (by $\hat{\beta}V/R$) vorticity field.

with multiple cyclones prescribed by Eq. 2, with one PC and eight (five) CPCs placed initially at the observed locations during Juno’s PJ4 orbit for the north (south) poles (Fig. 2a–b). For simplicity, and due to limited observational data, we assume identical cyclones. Due to this choice and the absence of small-scale forcing, the oscillatory motion discussed by *Gavriel and Kaspi (2022)* is not excited. Hence, we focus on reproducing the mean westward drift.

This model involves four unknown parameters: L_d , and the three cyclone profile parameters (R, V, b). To explore the phase space of this model, we use the Ultraneest library (*Buchner, 2021*), which employs a Bayesian nested sampling approach to identify the best-fitting solutions (*Buchner, 2023*). As a benchmark, we use the 5-year observed trajectories of the north and south polar cyclones (*Mura et al., 2022*) (Fig. 2a–b) to calculate the average westward drift between the cyclones. This value is then used to calculate a likelihood function that evaluates the probability of a parameter set being accurate, based on the resultant model westward drift (see supporting information for details on the numerical model, likelihood function, and model sampling).

We sampled 10,000 parameter sets, integrating each simulation for seven years and calculating the resultant mean westward drift between the cyclones during the last five years (where the first 2 years act as a spin-up). Illustrative model outputs (Fig. 2 panels e–g for the north pole and panels h–j for the south) span a variety of outcomes: drifts too fast (panels e, h), too slow (panels f, i), and mergers (panels g, j). Examples of parameter

sets that successfully recreate the observed drift are shown in Fig. 2c–d.

Due to intrinsic parameter degeneracies, the algorithm returns a posterior distribution rather than a specific set of parameters that matches the observed westward drift. From this distribution, we obtain a more realistic estimation for the deformation radius of $L_d = 192.41^{+47.13}_{-38.33}$ km and $L_d = 319.15^{+41.55}_{-33.45}$ km at the 1σ confidence level for the north and south poles (Fig. 2k), respectively. The resulting posterior distributions for R, V , and b (Fig. 2l–n) are consistent with plausible mean values for Jupiter’s polar cyclones and, interestingly, are very similar between the poles.

4 Interpreting the Vertical Structure of Jupiter’s Polar Atmosphere from the Drift Rate of the Polar Cyclones

The standard shallow-water (SW) expression for the deformation radius, $L_d = \sqrt{gH}/f_0$, is not well-suited to Jupiter’s upper atmosphere. This expression assumes a constant density and no vertical dependence of the flow, whereas Jupiter’s upper-atmospheric density increases exponentially with depth (*Guillot and Morel, 1995*) over many scale heights. To account for these vertical variations, we consider the full QG vorticity equation

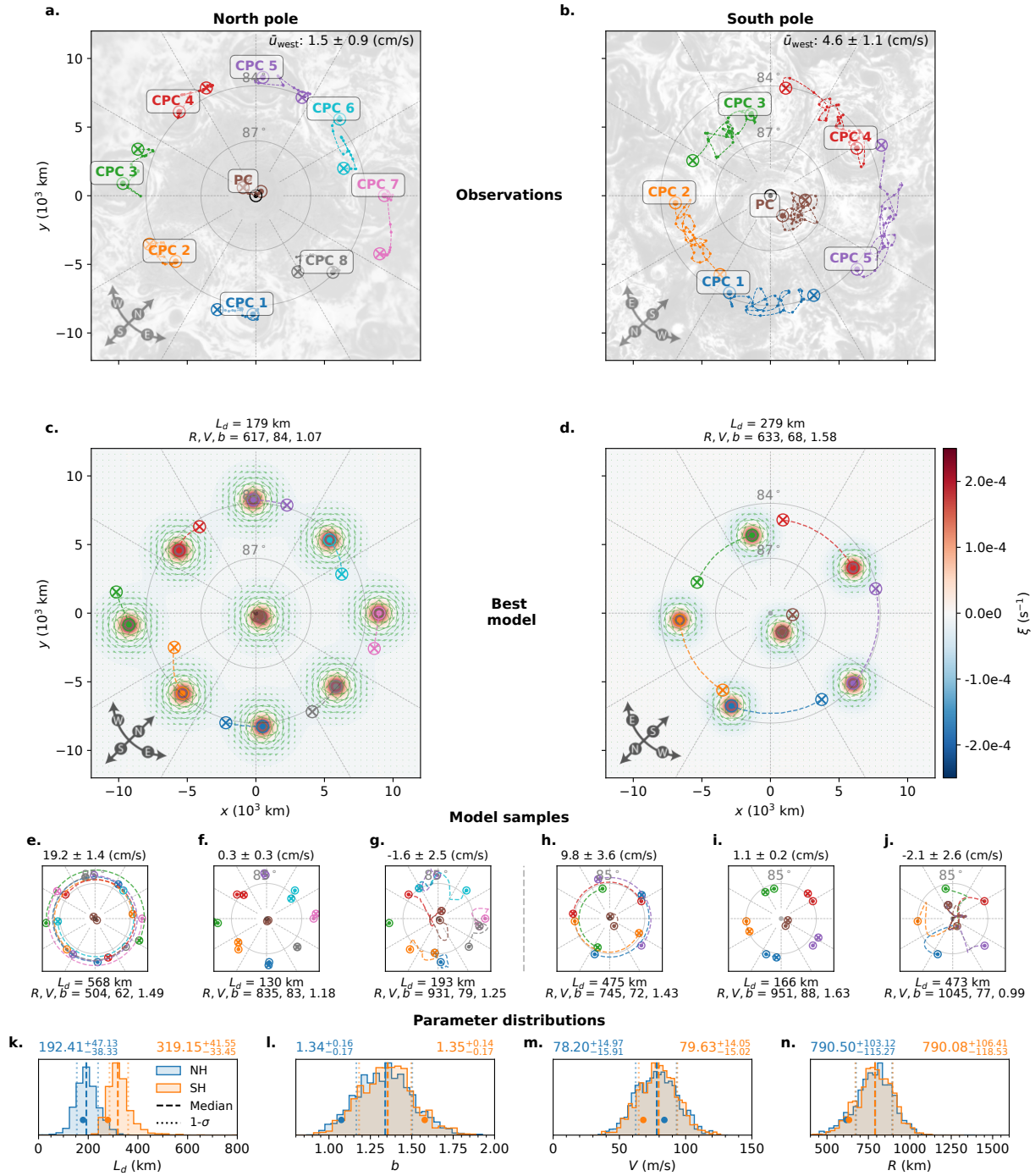


Figure 2: **Constraining L_d at Jupiter's Poles Using Observed and Simulated Cyclone Drifts.** (a,b) Observed trajectories of the north (a) and south (b) polar cyclones over five years (*Mura et al., 2022*). The \odot and \otimes symbols mark the start and end points, respectively. The background is a JIRAM infrared image from PJ4 (Image from *Adriani et al. (2018)*), corresponding to the onset of these trajectories. (c,d) Simulated trajectories after five years for a model that reproduces the observed mean westward drift. The color scale and green arrows show the vorticity and velocity fields at $t = 0$. (e–j) Sample model trajectories from the nested sampling routine, illustrating diverse outcomes. The numbers above the panels are the mean and standard deviation (between the cyclones) of the westward drift. The parameters used in each panel are listed below the panels. (k–n) Histogram plots of the posterior parameter distributions produced by Ultraneest (*Buchner, 2021*), after sampling 10,000 parameter sets per pole for the north (blue) and south (orange) polar cyclones. The dashed lines denote the median, and dotted lines mark the $\pm 1\sigma$ for the distributions. These values are written above the panels. The blue and orange points represent the values for the best model tracks (panels c,d).

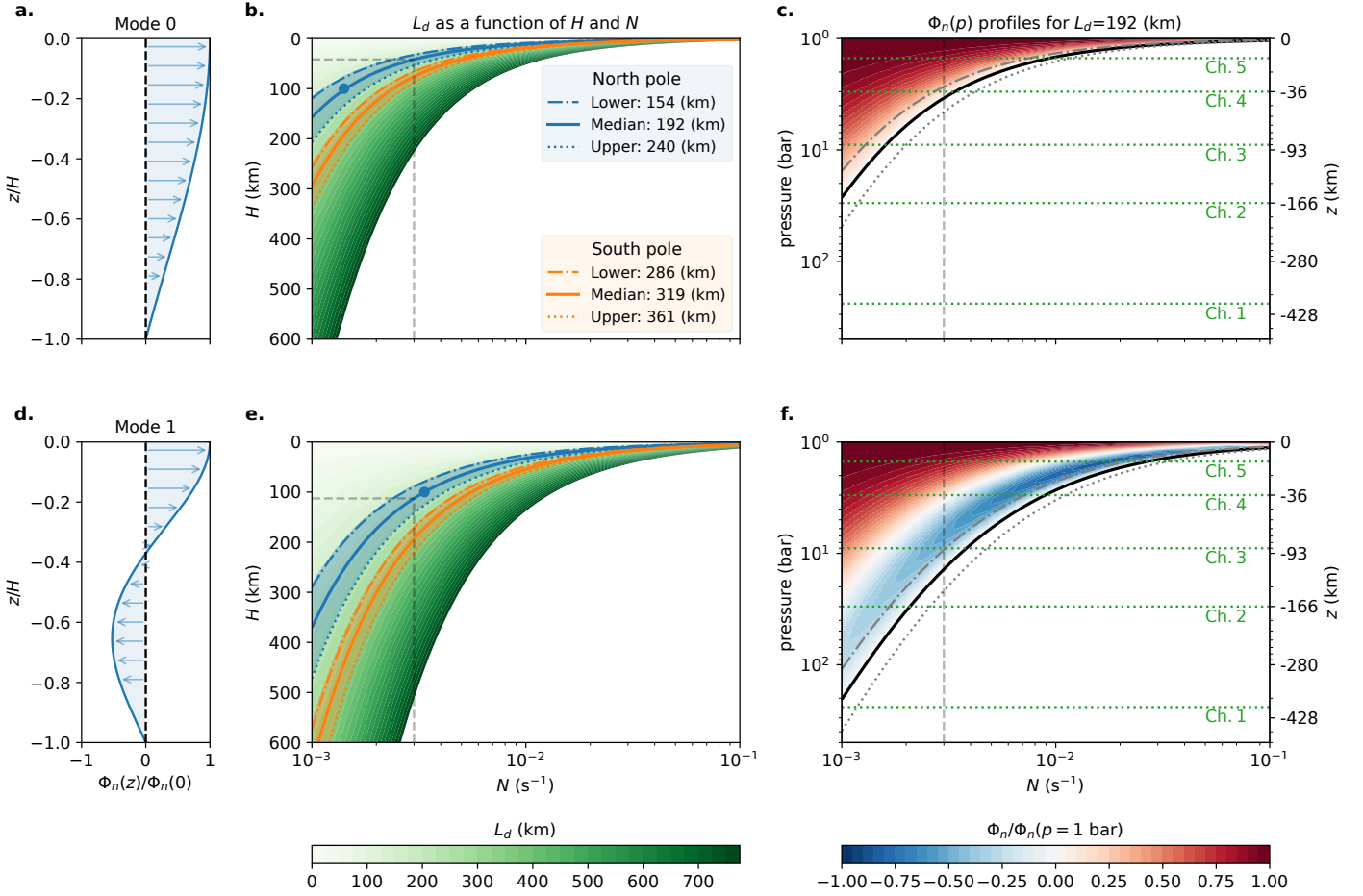


Figure 3: **Interpretation of the Cyclones' Vertical Structure from the Deformation Radius.** The first row corresponds to the "mode 0" solutions of the eigenvalue problem described by Eq. 6, while the second row corresponds to "mode 1". (a,d) Vertical profiles of Φ_n for each mode. (b,e) Solutions for L_d (green shades) for various combinations of N (Brunt-Väisälä frequency) and H (depth). The estimated L_d distributions from Fig. 2k are shown by the blue and orange curves for the north and south poles, respectively. (c,f) Solutions for Φ_n as a function of pressure below the cloud layer, following the N and H relationship indicated by the blue solid curve in panels (b) and (e). Green dotted lines indicate the maximum sensitivity depths of the MWR channels. The numbers on the right ordinate show the altitude relative to 1 bar. Grey dashed lines in panels (b,c,e,f) denote the values used to generate the profiles in panels (a) and (d), and to produce Fig. 4. The color along the grey dashed line in panels (c,f) corresponds to the $\Phi(z)$ profiles shown in panels (a,d).

(Vallis, 2017):

$$\frac{D}{Dt} \left(\nabla^2 \psi + f + \frac{f_0^2}{\bar{\rho}} \frac{\partial}{\partial z} \left(\frac{\bar{\rho}}{N^2} \frac{\partial \psi}{\partial z} \right) \right) = 0, \quad (4)$$

where N is the Brunt-Väisälä frequency, indicating the stability of the atmosphere with respect to vertical motion, and $\bar{\rho}$ is the density profile.

To account for variations in the vertical direction, we assume the streamfunction can be separated into horizontal and vertical components:

$$\psi(x, y, z, t) = \sum_n \psi_n(x, y, t) \Phi_n(z) \quad (5)$$

where $\Phi_n(z)$ is the vertical profile (or "mode") for each n . Substituting this form into the QG equations requires each Φ_n to

satisfy the vertical eigenvalue problem:

$$\frac{f_0^2}{\bar{\rho}} \frac{\partial}{\partial z} \left(\frac{\bar{\rho}}{N^2} \frac{\partial \Phi_n}{\partial z} \right) + \Gamma_n \Phi_n = 0, \quad (6)$$

where Γ_n is an eigenvalue. For each mode n , the corresponding deformation radius is given by $L_{d,(n)} = \Gamma_n^{-\frac{1}{2}}$. Under the assumption that the cyclones are dominated by a single vertical mode the horizontal dynamics derived from the two-dimensional QG equation (Eq. 3), and the full three-dimensional QG equation (Eq. 4) will yield the same horizontal dynamics for the given $L_{d,(n)}$. Given our estimation of the L_d value required to achieve the observed westward drift (Fig. 3), we can use the eigenvalue problem posed by Eq. 6 to investigate which vertical structures (eigenfunctions $\Phi_n(z)$) satisfy the required L_d .

We solve this eigenvalue problem using the Dedalus library (Burns et al., 2020), applying boundary conditions of no vertical velocity at the tropopause ($\partial_z \Phi_n|_{z=0} = 0$) and no flow at the bottom ($\Phi_n|_{z=-H} = 0$). For $\bar{\rho}(z)$, we adopt a reference density profile estimated by internal models of Jupiter, constrained by an AI-based parameter sweep (Ziv et al., 2024a,b). We focus here on the lowest two modes ($n = \{0, 1\}$), which are illustrated in Fig. 3(a,d). The $n = 0$ mode corresponds to a simple decay profile, whereas $n = 1$ changes signs along the column.

Since Eq. 6 depends only on N (assumed constant here) and H , we present $L_{d,(n)}$ solutions as a function of these two parameters in Fig. 3(b,e), for both modes. The constrained range of deformation radii from the previous section (Fig. 2) is indicated for the north (blue) and south (orange) poles, essentially giving an H as a function of N for each pole. Focusing on the relationship defined by the blue solid curve in Fig. 3(b,e), we plot the corresponding $\Phi_n(z)$ profiles as a function of pressure below the cloud level for different N values (Fig. 3(c,f)).

The MWR instrument, expected to probe below Jupiter’s clouds at the north pole in the near future, measures brightness temperature at six channels. The maximum sensitivity pressure levels for each MWR channel are marked by green dotted lines, with Channel 6 above the 1-bar level. For a plausible range $N = 3 - 20 \times 10^{-3} \text{ s}^{-1}$ (Lee and Kaspi, 2021), and focusing first on mode 0, we anticipate that the polar cyclones’ footprint will be visible in Channels 6 and 5 (and Channel 4 if $N \approx 0.3 \times 10^{-2} \text{ s}^{-1}$). However, if the real Jovian poles exhibit turbulence with a vertical phase shift—reminiscent of terrestrial storms with low-level convergence and upper-level divergence—then mode 1 may also be excited. In that scenario, signatures could extend into Channel 3 for the same range of N s.

Figure 4 illustrates an example of how ψ extends downward and intersects with the MWR channels for $N = 3 \times 10^{-3} \text{ s}^{-1}$, the lower bound reported in Lee and Kaspi (2021). Channel 6, sensitive to pressures around 0.7 bar, lies slightly above the eigenfunctions’ range (which starts near 1 bar). We assume that Channel 6 will display a ψ field similar to that of Channel 5. The JIRAM background photograph (Adriani et al., 2018) represents the cloud deck at approximately this pressure level. The downward extension of ψ below Channel 4 depends on the excitation of mode 1. It is important to note that the MWR mea-

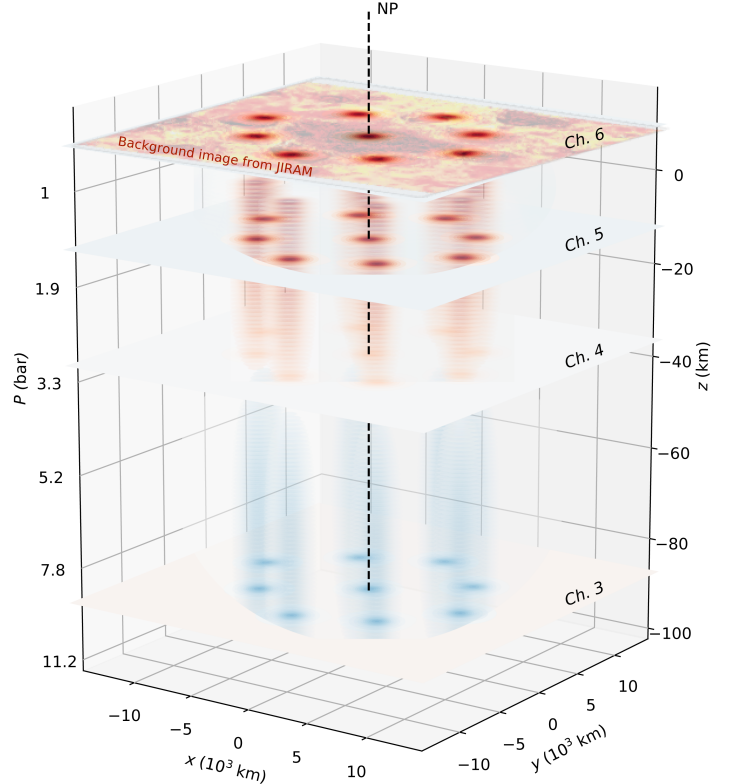


Figure 4: **Vertical Structure and Intersections with Instrument Sensitivity Depths at the North Pole.** The ψ field from Fig. 2c was extended downward using the eigenfunctions from Fig. 3a,d, which correspond to $N = 3 \times 10^{-3} \text{ (s}^{-1}\text{)}$ and $H = 41.7$ (112.7) km for mode 0 (mode 1). Both modes yield $L_d = 192$ km, with mode 0 terminating ($\psi = 0$) at $z = -41.7$ km, and mode 1 continuing further to $\psi = 0$ at $z = -112.7$ km. The planes represent ψ at the MWR channels that overlap with the eigenfunction range, while the shaded regions between the planes depict ψ values between the channels. The dashed black line indicates the north pole. The background image on channel 6 is a JIRAM measurement from PJ4 (Adriani et al., 2018), similar to Fig. 2a.

asures brightness temperature, which is only indirectly related to ψ . Predicting MWR observations requires a layer of translation, involving solutions for vertical velocity and the subsequent diffusion-advection of ammonia, given the background ammonia distribution (Duer et al., 2021).

5 Discussion

In this study, we examined how the vertical extent of polar cyclones influences their vorticity-driven motion (Fig. 1). Our analysis demonstrated that shallower cyclones undergo a weaker

β -drift, which explains the order-of-magnitude discrepancy between the observed westward drift of the south-polar cyclones and the much faster rates anticipated by an idealized, infinitely deep model (Gavriel and Kaspi (2023), their Fig. 2).

We then employed a 2D polar model initialized with identical cyclones at their observed locations (during PJ4). This model provides a dynamical constraint on the deformation radius, L_d , which encodes information about the cyclones' vertical structure. We found that both excessively large and excessively small values of L_d produce westward drifts that deviate strongly from observations. A sampling algorithm estimates $L_d \sim 200$ (km) at the north pole and ~ 300 (km) at the south pole. While the posterior distributions of L_d at the two poles do overlap, it remains an open question whether genuine differences in L_d exist between the poles, given Jupiter's negligible obliquity and the resulting expected near-symmetry. However, the indicated difference in L_d between the poles could have important implications for the cyclones' characteristics. Specifically, the smaller L_d at the north pole might place a constraint on the maximum possible size of the north polar cyclones, leading to their smaller size and, consequently, a larger number of cyclones.

Using these estimates of L_d , we sought consistency between the 2D QG framework (Fig. 2) and a 3D QG model that incorporates density variations with depth (Eq. 4). This required solving the eigenvalue problem in Eq. 6, in which the eigenvalues yield L_d for different vertical modes, and the numerically determined eigenfunctions describe the cyclone's vertical structure relative to the cloud deck. In our idealized approach, we assumed a constant Brunt-Väisälä frequency, N , and a single dominant vertical mode, both of which can introduce some uncertainty. The solutions (Fig. 3) suggest that for $N \approx 10^{-2} \text{ s}^{-1}$, cyclone depths of 10 – 80 km at the north pole and 20 – 120 km at the south pole are plausible, depending on the mode. If $N \approx 10^{-3} \text{ s}^{-1}$, the estimated cyclone depths increase substantially, ranging 100 – 450 km at the north pole and 200 – 600 km at the south pole.

These results (Fig. 3, 4) also establish a framework for interpreting forthcoming measurements from Juno's MWR at Jupiter's north pole (Orton et al., 2024). Once these measurements become available, our model can be used to connect each channel's footprint to the underlying vertical structure and static stability N . In a subsequent analysis, one can investigate how the cyclonic circulations drive vertical transport and ammonia redistribution, following an approach akin to that used in the study of Jupiter's Ferrel-cell circulation (Duer et al., 2021).

In summary, our work offers a novel way to bridge observed cloud-level motions and the deeper structure of Jovian polar cyclones. The constraints we derive on the deformation radius, vertical structure, and static stability at Jupiter's poles can guide future studies aimed at modeling the energy fluxes responsible for the formation and maintenance of these cyclones against dissipation. By linking the deformation radius derived from β -drift constraints to vertical modes in a 3D QG framework, we gain a clearer understanding of how these cyclones might extend be-

low the visible cloud layer, and how their vertical structure governs their horizontal drift.

Open Research

The data analyzed in this study were published by Ref. (Mura et al., 2022) (DOI: <https://doi.org/10.1029/2022JE007241>), as cited in the text. The simulations were run with the Dedalus solver (Burns et al., 2020) (DOI: <https://doi.org/10.1103/PhysRevResearch.2.023068>).

Acknowledgments

This research has been supported by the Helen Kimmel Center for Planetary Science at the Weizmann Institute of Science. We thank Rei Chemke, Keren Duer, Eli Galanti and Or Hadas for insightful conversations and helpful feedback.

Competing Interests

Authors declare that they have no competing interests.

References

- Adem, J., A series solution for the barotropic vorticity equation and its application in the study of atmospheric vortices, *Tellus*, 8(3), 364–372, 1956.
- Adriani, A., et al., JIRAM, the Jovian Infrared Auroral Mapper, *Space Science Reviews*, 213(1), 393–446, 2017.
- Adriani, A., et al., Clusters of cyclones encircling Jupiter's poles, *Nature*, 555(7695), 216–219, 2018.
- Adriani, A., et al., Two-year observations of the Jupiter polar regions by JIRAM on board Juno, *J. Geophys. Res. (Planets)*, p. e2019JE006098, 2020.
- Atreya, S. K., M. H. Wong, T. C. Owen, P. R. Mahaffy, H. B. Niemann, I. de Pater, P. Drossart, and T. Encrenaz, A comparison of the atmospheres of Jupiter and Saturn: deep atmospheric composition, cloud structure, vertical mixing, and origin, *Planetary and Space Science*, 47(10), 1243–1262, 1999.
- Benzeggouta, D., B. Favier, and M. Le Bars, Laboratory model for barotropic vortices drifting towards a planetary pole, *Physical Review Fluids*, 10(1), 014,701, 2025.
- Bolton, S. J., et al., Jupiter's interior and deep atmosphere: The initial pole-to-pole passes with the Juno spacecraft, *Science*, 356(6340), 821–825, 2017.
- Bolton, S. J., et al., Microwave observations reveal the deep extent and structure of Jupiter's atmospheric vortices, *Science*, 374(6570), 968–972, 2021.

- Brueshaber, S. R., K. M. Sayanagi, and T. E. Dowling, Dynamical regimes of giant planet polar vortices, *Icarus*, 323, 46–61, 2019.
- Buchner, J., Ultranest—a robust, general purpose Bayesian inference engine, *arXiv preprint arXiv:2101.09604*, 2021.
- Buchner, J., Nested sampling methods, *Statistic Surveys*, 17, 169–215, 2023.
- Burns, K. J., G. M. Vasil, J. S. Oishi, D. Lecoanet, and B. P. Brown, Dedalus: A flexible framework for numerical simulations with spectral methods, *Physical Review Research*, 2(2), 023,068, 2020.
- Chan, J. C. L., and R. T. Williams, Analytical and numerical studies of the beta-effect in tropical cyclone motion. part i: Zero mean flow, *Journal of the Atmospheric Sciences*, 44(9), 1257–1265, 1987.
- de Pater, I., R. J. Sault, B. Butler, D. DeBoer, and M. H. Wong, Peering through Jupiter’s clouds with radio spectral imaging, *Science*, 352(6290), 1198–1201, 2016.
- Duer, K., E. Galanti, and Y. Kaspi, Gas giant simulations of eddy-driven jets accompanied by deep meridional circulation, *AGU Advances*, 4(6), e2023AV000,908, 2023.
- Duer, K., et al., Evidence for multiple Ferrel-like cells on Jupiter, *Geophysical Research Letters*, 48(23), e2021GL095,651, 2021.
- Fletcher, L. N., et al., Jupiter’s temperate belt/zone contrasts revealed at depth by Juno microwave observations, *Journal of Geophysical Research: Planets*, 126(10), e2021JE006,858, 2021.
- Franklin, J. L., S. E. Feuer, J. Kaplan, and S. D. Aberson, Tropical cyclone motion and surrounding flow relationships: Searching for beta gyres in omega dropwindsonde datasets, *Monthly Weather Review*, 124(1), 64–84, 1996.
- Galanti, E., Y. Kaspi, F. J. Simons, D. Durante, M. Parisi, and S. J. Bolton, Determining the depth of Jupiter’s Great Red Spot with Juno: a Slepian approach, *The Astrophysical Journal*, 874(2), L24, 2019.
- Galanti, E., et al., Constraints on the latitudinal profile of Jupiter’s deep jets, *Geophysical Research Letters*, 48(9), e2021GL092,912, 2021.
- Gavriel, N., and Y. Kaspi, The number and location of Jupiter’s circumpolar cyclones explained by vorticity dynamics, *Nature Geoscience*, 14(8), 559–563, 2021.
- Gavriel, N., and Y. Kaspi, The oscillatory motion of jupiter’s polar cyclones results from vorticity dynamics, *Geophysical Research Letters*, 49(15), e2022GL098,708, 2022.
- Gavriel, N., and Y. Kaspi, The westward drift of Jupiter’s polar cyclones explained by a center-of-mass approach, *Geophysical Research Letters*, 50(19), e2023GL103,635, 2023.
- Guillot, T., and P. Morel, CEPAM: a code for modeling the interiors of giant planets., *Astron. and Astro. Supp. ser.*, 109, 109–123, 1995.
- Hyder, A., W. Lyra, N. Chanover, R. Morales-Juberías, and J. Jackiewicz, Exploring Jupiter’s Polar Deformation Lengths with High-resolution Shallow Water Modeling, *The Planetary Science Journal*, 3(7), 166, 2022.
- Janssen, M. A., et al., MWR: Microwave Radiometer for the Juno Mission to Jupiter, *Space Science Reviews*, 213(1-4), 139–185, 2017.
- Kaspi, Y., et al., Jupiter’s atmospheric jet streams extend thousands of kilometres deep, *Nature*, 555(7695), 223–226, 2018.
- Kaspi, Y., et al., Observational evidence for cylindrically oriented zonal flows on Jupiter, *Nature Astronomy*, 7(12), 1463–1472, 2023.
- Lam, J. S.-L., and D. G. Dritschel, On the beta-drift of an initially circular vortex patch, *Journal of Fluid Mechanics*, 436, 107–129, 2001.
- Lee, S., and Y. Kaspi, Towards an understanding of the structure of Jupiter’s atmosphere using the ammonia distribution and the transformed eulerian mean theory, *Journal of the Atmospheric Sciences*, 2021.
- Li, C., A. P. Ingersoll, A. P. Klipfel, and H. Brettle, Modeling the stability of polygonal patterns of vortices at the poles of Jupiter as revealed by the Juno spacecraft, *Proceedings of the National Academy of Sciences*, 117(39), 24,082–24,087, 2020.
- Li, C., et al., The distribution of ammonia on Jupiter from a preliminary inversion of Juno microwave radiometer data, *Geophysical Research Letters*, 44(11), 5317–5325, 2017.
- Mura, A., et al., Oscillations and stability of the Jupiter polar cyclones, *Geophysical Research Letters*, 48(14), e2021GL094,235, 2021.
- Mura, A., et al., Five years of observations of the circumpolar cyclones of Jupiter, *Journal of Geophysical Research: Planets*, 127(9), e2022JE007,241, 2022.
- O’Neill, M. E., K. A. Emanuel, and G. R. Flierl, Polar vortex formation in giant-planet atmospheres due to moist convection, *Nature Geoscience*, 8(7), 523–526, 2015.
- Orton, G., et al., Unexpected results from microwave sounding of Jupiter’s north polar cyclones, *Tech. rep.*, 2024.
- Parisi, M., et al., The depth of Jupiter’s Great Red Spot constrained by Juno gravity overflights, *Science*, 374(6570), 964–968, 2021.

- Siegelman, L., W. R. Young, and A. P. Ingersoll, Polar vortex crystals: Emergence and structure, *Proceedings of the National Academy of Sciences*, 119(17), e2120486, 119, 2022a.
- Siegelman, L., et al., Moist convection drives an upscale energy transfer at Jovian high latitudes, *Nature Physics*, pp. 1–5, 2022b.
- Smith, R. K., An analytic theory of tropical-cyclone motion in a barotropic shear flow, *Quarterly Journal of the Royal Meteorological Society*, 117(500), 685–714, 1991.
- Smith, R. K., and W. Ulrich, An analytical theory of tropical cyclone motion using a barotropic model, *Journal of the Atmospheric Sciences*, 47(16), 1973–1986, 1990.
- Sutyrin, G. G., and G. R. Flierl, Intense vortex motion on the beta plane: Development of the beta gyres, *Journal of the Atmospheric Sciences*, 51(5), 773–790, 1994.
- Vallis, G. K., *Atmospheric and oceanic fluid dynamics*, Cambridge University Press, 2017.
- Young, R. E., The galileo probe mission to Jupiter: Science overview, *Journal of Geophysical Research: Planets*, 103(E10), 22,775–22,790, 1998.
- Ziv, M., E. Galanti, S. Howard, T. Guillot, and Y. Kaspi, Characterizing Jupiter’s interior using machine learning reveals four key structures, *Astronomy & Astrophysics*, 692, A251, 2024a.
- Ziv, M., E. Galanti, A. Sheffer, S. Howard, T. Guillot, and Y. Kaspi, NeuralCMS: A deep learning approach to study Jupiter’s interior, *Astronomy & Astrophysics*, 686, L7, 2024b.

Supporting Information

Developing a Model Following a Cyclone That Includes the Effect of Stretching

This section provides additional details for the model used to generate Fig. 1. We first derive the governing vorticity equation in a moving reference frame centered on the vortex, then describe the numerical setup and present key aspects of the simulation results.

Deriving the Model Equation

In this subsection, we derive the vorticity equation with moving coordinates originating in the vortex's center. The model, inspired by (Smith, 1991), assumes a β plane, and one layer of fluid with a constant density.

We begin with the single-layer shallow-water (SW) quasi-geostrophic (QG) vorticity equation on a β plane (Vallis, 2017):

$$\frac{D}{Dt} \left(\xi + \beta y - \frac{1}{L_d^2} \psi \right) = 0, \quad (\text{S1})$$

where

$$\frac{D}{Dt} = \left(\frac{\partial}{\partial t} + \mathbf{u} \cdot \nabla \right), \quad (\text{S2})$$

\mathbf{u} is the velocity vector, $\xi = \nabla \times \mathbf{u}$ is the relative vorticity, and β is the constant meridional gradient of the planetary vorticity (f) or any prescribed background vorticity gradient.

Scaling the Equation We non-dimensionalize using the following scales:

$$\begin{aligned} (x, y) &= R(\hat{x}, \hat{y}), \quad t = \frac{R}{V}\hat{t}, \\ \mathbf{u} &= V\hat{\mathbf{u}}, \quad \xi = \frac{V}{R}\hat{\xi}, \quad \psi = VR\hat{\psi}, \end{aligned} \quad (\text{S3})$$

where R and V are the characteristic length and velocity scales of the vortex. In these non-dimensional variables, the vorticity equation becomes

$$\frac{D}{Dt} \left(\xi + \hat{\beta} y \right) - \frac{1}{\text{Bu}} \frac{\partial \psi}{\partial t} = 0, \quad (\text{S4})$$

where

$$\hat{\beta} \equiv \frac{\beta R^2}{V}, \quad \text{Bu} \equiv \frac{L_d^2}{R^2} = \frac{gH}{R^2 f_0^2}, \quad (\text{S5})$$

and $\hat{\beta}$ is a small number, representing the magnitude of β -drift. This non-dimensional number can be intuitively understood as a ratio between the change in vorticity across the vortex ($\delta f = \beta R$) and the vortex's relative vorticity scale (V/R).

Moving to a Coordinate System That Drifts With the Vortex We shift to a moving coordinate system (x_β, y_β) such that

$$\begin{aligned} x &= x_\beta + \int_0^t \hat{\beta} u_\beta dt, \\ y &= y_\beta + \int_0^t \hat{\beta} v_\beta dt, \end{aligned} \quad (\text{S6})$$

where $\hat{\beta} \mathbf{u}_\beta = \hat{\beta} (u_\beta, v_\beta)$ is the beta-drift speed, changing only with time, and (x_β, y_β) is a new coordinate system that moves with \mathbf{u}_β . By the chain rule (with subscript 0 for the stationary frame):

$$\frac{\partial \psi}{\partial t_0} = \frac{\partial \psi}{\partial t} - \hat{\beta} u_\beta \frac{\partial \psi}{\partial x_\beta}, \quad (\text{S7})$$

so the material derivative becomes

$$\frac{D_0}{Dt} = \frac{\partial}{\partial t} + \left(\mathbf{u} - \hat{\beta} \mathbf{u}_\beta \right) \cdot \nabla_\beta, \quad (\text{S8})$$

where ∇_β is a gradient in the moving coordinates. In the moving coordinates, the vorticity equation becomes

$$\left[\frac{\partial}{\partial t} + \left(\mathbf{u} - \hat{\beta} \mathbf{u}_\beta \right) \cdot \nabla_\beta \right] \left(\xi + \hat{\beta} \left[y + \hat{\beta} \int_0^t v_\beta dt \right] \right) - \frac{1}{\text{Bu}} \left(\frac{\partial \psi}{\partial t} - \hat{\beta} \mathbf{u}_\beta \cdot \nabla_\beta \psi \right) = 0. \quad (\text{S9})$$

We then decompose the fields into a fixed (vortex) component and a perturbation (or generated) component:

$$f = f_v(x_\beta, y_\beta) + \hat{\beta} f_g(x_\beta, y_\beta, t). \quad (\text{S10})$$

After dividing by $\hat{\beta}$ and retaining terms at leading order, we obtain

$$\frac{\partial}{\partial t} \left(\xi_g - \frac{\psi_g}{\text{Bu}} \right) = -v_v - \mathbf{u}_v \cdot \nabla \xi_g - (\mathbf{u}_g - \mathbf{u}_\beta) \cdot \nabla \xi_v - \frac{1}{\text{Bu}} \mathbf{u}_\beta \cdot \nabla \psi_v + O(\hat{\beta}) = 0, \quad (\text{S11})$$

while noting that due to the symmetry of the constant vortex profile, advective terms $\mathbf{u}_v \cdot \nabla(\psi_v$ or $\xi_v)$ are zero. This equation represents a potential vorticity equation for the evolution of a velocity field generated by β -drift in a moving frame. The velocity vector, $\mathbf{u}_\beta \approx \mathbf{u}_g(0, 0, t)$ is the generated velocity at the vortex center, and $\mathbf{u}_v, \xi_v, \psi_v$ are determined by the chosen vortex profile.

The version of Eq. S11 presented in the main text (Eq. 1) is simplified for focusing the reader's attention on the important points. It unscales back the "g" variables by $\hat{\beta}$, so as to directly see the dependence of β -drift on $\hat{\beta}$, and assumes that the terms $((\mathbf{u}_g - \mathbf{u}_\beta) \cdot \nabla \xi_v, -\frac{1}{\text{Bu}} \mathbf{u}_\beta \cdot \nabla \psi_v)$ are relatively small. This assumption can be intuitively understood at the beginning of the motion, where $\mathbf{u}_g = \mathbf{u}_\beta = 0$. Nonetheless, the simulations (Fig. 1) use the full version (Eq. S11).

Numerical Model Setup

For solving Eq. S11 we use the Dedalus PDE solver (*Burns et al., 2020*) with double periodic bases. To enforce a concentric boundary, we set the (scaled) domain size as $(x, y) \in \{-20, 20\}$ and add a relaxation term of the form

$$\frac{\xi_g}{\tau_d} G(r, R_d, A_d), \quad (\text{S12})$$

where $\tau_d = 0.1\pi$ is the relaxation time scale,

$$G = \frac{1}{2} (1 - \tanh(A_d(R_d - r))) \quad (\text{S13})$$

is a continuous activation function, $r = \sqrt{x^2 + y^2}$ is the radius from the pole, $A_d = 20$ is the sharpness of the transition to the relaxation zone, and $R_d = 15$ is the activation radius. We also added a viscosity term of the form $\text{Ek} \nabla^4 \psi_g$, with $\text{Ek} = 0.01$, for stability. A resolution of 96×96 grid points was sufficient for the parameter sweep (Fig. 1).

The vortex profile (compare to Eq. 2 in the main text, here in scaled variables) is taken as (*Chan and Williams, 1987*)

$$\xi_v = (2 - r^b) e^{\frac{1}{b}(1-r^b)}, \quad (\text{S14})$$

where b controls how sharply the tangential velocity changes with radius. From ξ_v , we obtain ψ_v by solving the Poisson equation $\nabla^2 \psi_v = \xi_v$.

In Fig. 1(a-b), we plot the resulting (u_β, v_β) with $b = 1.2$ and four values of Bu. We find that u_β behaves like an exponential decay function, $u_\beta \sim A(1 - e^{-t/\tau})$, where the amplitude A and timescale τ minimize the root-mean-square error (RMSE) relative to the simulated u_β . This parameterization allows for a simple presentation of the behavior of u_β as a function of Bu (Fig. 1c).

The Polar QG Model

In this section, we present the details of the polar quasi-geostrophic (QG) model and the statistics underlying the results shown in Fig. 2. We solve the SW-QG equation (*Vallis, 2017*),

$$\frac{D}{Dt} \left(\nabla^2 \psi + f - \frac{1}{L_d^2} \psi \right) = 0, \quad (\text{S15})$$

where

$$f = 2\Omega \cos \left(\frac{\sqrt{x^2 + y^2}}{R_J} \right), \quad (\text{S16})$$

$\Omega = 1.759 \times 10^{-4}$ is Jupiter's rotation rate, and $R_J = 66,854$ km is Jupiter's radius. In practice, our model solves the non-dimensional form of Eq. S15:

$$\frac{D}{Dt} \left(\nabla^2 \psi + \hat{f} - \frac{1}{\text{Bu}} \psi \right) = \text{Ek} \nabla^4 \psi, \quad (\text{S17})$$

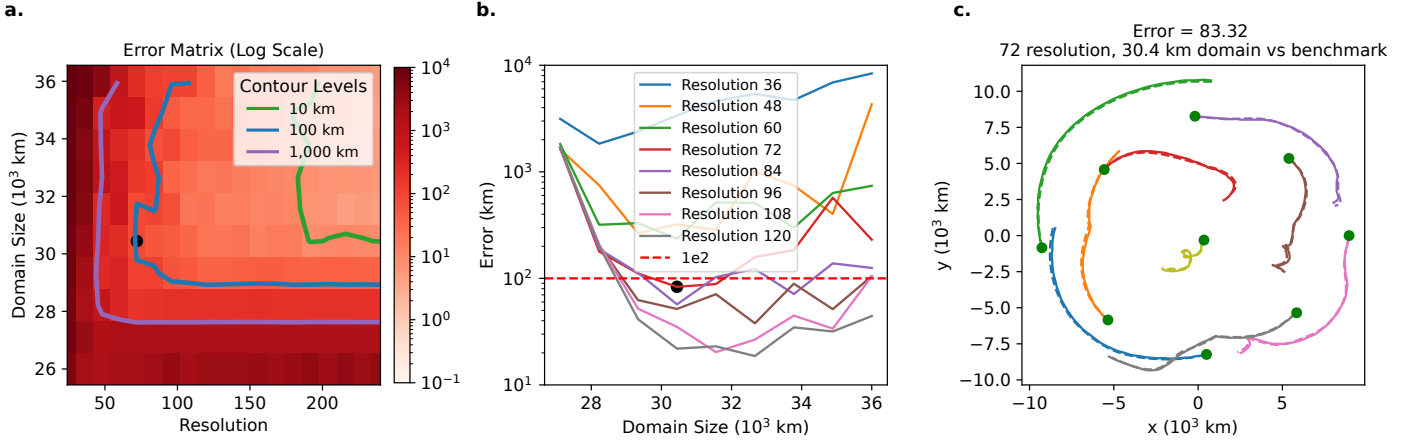


Figure S1: **Analyzing the required resolution and domain size for sampling the model.** (a) Contours of RMSE (in km) between each model’s cyclone trajectories and the benchmark, as functions of resolution (abscissa) and domain size (ordinate). The blue contour highlights the 100 km threshold for acceptable error. The black dot is the chosen setting. (b) RMSE dependence on domain size for selected resolutions. (c) Benchmark trajectories (solid lines) compared with those at the chosen 72×72 resolution and a 30,400 km domain (dashed lines).

where lengths are scaled by $L = 1,000$ km and velocities by $U = 50$ m s⁻¹. Thus, time is scaled by $T = L/U$. The non-dimensional variables are $\hat{\psi} = \frac{1}{LU} \psi$ and $\hat{f} = \frac{L}{U} G(r, R_d, A_d) f$. We set the numerical viscosity to $\text{Ek} = 10^{-5}$, and the Burger number is $\text{Bu} = (L_d/L)^2$, where L_d is an input parameter.

We solve the model using Dedalus (Burns *et al.*, 2020) on a doubly periodic Fourier domain. The initial condition consists of N_{cyc} cyclones (9 for the north pole and 6 for the south pole) of the form (in dimensional variables):

$$\xi = \sum_{n=1}^{N_{\text{cyc}}} \frac{V}{R} \left(2 - \left(\frac{r_n}{R} \right)^b \right) \exp \left[\frac{1}{b} \left(1 - \left(\frac{r_n}{R} \right)^b \right) \right], \quad (\text{S18})$$

where $r_n = \sqrt{(x - x_n)^2 + (y - y_n)^2}$ measures the distance from the center of cyclone n . The cyclone centers $\{(x_n, y_n)\}$ are taken from Juno PJ4 observations (Mura *et al.*, 2022). We obtain the initial streamfunction by solving $\nabla^2 \psi = \xi$ prior to each run.

To mitigate boundary effects from the rectangular domain, we use the "trap" method (Siegelman *et al.*, 2022a). Specifically, we multiply the planetary PV by an activation function (Eq. S13) which smoothly transitions from ≈ 0 outside $r > R_d$ to $\approx \frac{L}{U} f$ inside $r < R_d$. In this study, we use $A_d = -20$ (negative values switch the domain of activation to within the circle), and choose R_d to be 97% of the total domain size. This procedure effectively "disconnects" the dynamics of interest (inside R_d) from the spurious influence of the periodic boundaries (outside R_d). Throughout each simulation, we track the centers of the cyclones in time and maintain their individual identities, thereby obtaining a record of their trajectories and possible mergers.

Sensitivity to Resolution and Domain Size

Because we sample the model repeatedly, we first identified the smallest resolution and domain size that would produce acceptably accurate cyclone trajectories. As a benchmark, we ran a high-resolution model (360×360 grid points) with a large domain (36,000 km on each side). We initialized nine identical cyclones at the north polar PJ4 positions ($L_d = 348$ km, $R = 867$ km, $V = 86.13$ m s⁻¹, $b = 1.51$), and integrated for 2,500 days.

Next, we reran the model at coarser resolutions and smaller domain sizes. For each simulation, we computed the RMSE between the resulting cyclone trajectories and those from the benchmark (Fig. S1). We are primarily interested in the average westward drift of these cyclones, so we allowed a maximum mean trajectory error of 100 km (blue contour in Fig. S1a). We found that a 72×72 grid with a domain size of 30,400 km satisfies this requirement. Figure S1b,c illustrates that the associated trajectories agree well with the benchmark. We therefore adopted these numerical settings for the sampling runs used to generate Fig. 2.

The Sampling Algorithm

To constrain L_d (the deformation radius) for Jupiter’s north and south poles using the observed westward drift rates, we apply Bayesian nested sampling via the ULtranest library (Buchner, 2021). This algorithm explores parameter space efficiently and

returns a posterior distribution of unknown parameters.

While noting that the model is idealized, and that we assume equivalent cyclones in order to drastically reduce the number of unknown variables, we are left with the 3 cyclone variables (R, V, b) and L_d as our 4 unknown variables. We assume the following normal priors:

$$\begin{aligned} L_d &\sim \mathcal{N}(400, 150^2) \quad (\text{km}), \\ b &\sim \mathcal{N}(1.2, 0.2^2), \\ U &\sim \mathcal{N}(80, 15^2) \quad (\text{m/s}), \\ R &\sim \mathcal{N}(900, 150^2) \quad (\text{km}). \end{aligned} \tag{S19}$$

We construct the likelihood function with two components. The first term,

$$C_1 = -\frac{1}{2} \left(\frac{\overline{\text{WW}}_O - \overline{\text{WW}}_M}{5 \times 10^{-3} \text{ m s}^{-1}} \right)^2 \tag{S20}$$

penalizes deviations between the observed mean westward drift $\overline{\text{WW}}_O$ and the model's mean drift $\overline{\text{WW}}_M$. The observed drift is averaged over five years and N_{cyc} cyclones, while the model drift is averaged over five years after a two-year spinup. The drifts are calculated like in *Gavriel and Kaspi (2023)*, without taking differences between the observed cyclones into account.

The second term,

$$C_2 = -\frac{1}{2} \left(\frac{N_{\text{mergers}}}{2} \right)^2, \tag{S21}$$

penalizes runs producing cyclones that merge. We simulate seven years of model time in snapshots spaced 53 days apart (approximately the period of Juno's orbits). Each "missing" cyclone (due to merger) in a snapshot contributes to N_{mergers} . Models with more frequent or earlier mergers thus have increasingly negative C_2 .

These two components combine additively:

$$C = C_1 + C_2, \tag{S22}$$

and we use this total likelihood to guide the nested-sampling algorithm. Each pole (north and south) is sampled with 10,000 allowed evaluations, yielding the posterior distributions presented in Fig. 2k-n.